



# Contributions of poly(3-hexylthiophene) nanowires to alteration of vertical inhomogeneity of bulk-heterojunction active layers and improvements of light-harvesting and power-conversion efficiency of organic solar cells

Sung-yoon Joe<sup>a, b</sup>, Shinyoung Ryu<sup>a, b</sup>, Duc Cuong Nguyen<sup>a, b</sup>, Jong Hyuk Yim<sup>a, b</sup>, Huiseong Jeong<sup>a, b</sup>, Na Young Ha<sup>a, b</sup>, Y.H. Ahn<sup>a, b</sup>, Ji-yong Park<sup>a, b</sup>, Soonil Lee<sup>a, b, \*</sup>

<sup>a</sup> Department of Physics, Ajou University, Suwon 443-749, South Korea

<sup>b</sup> Department of Energy Systems Research, Ajou University, Suwon 443-749, South Korea

## ARTICLE INFO

### Article history:

Received 30 November 2016

Received in revised form

31 December 2016

Accepted 31 December 2016

Available online 3 January 2017

### Keywords:

Poly(3-hexylthiophene-2,5-diyl) nanowire

Indene-C60 bisadduct

Bulk heterojunction

Organic solar cell

Light harvesting efficiency

## ABSTRACT

We report a 47.1% efficiency improvement resulting from the combination of device-architecture modification and inclusion of poly(3-hexylthiophene-2,5-diyl) nanowires (P3HT NWs) in bulk heterojunction (BHJ) active layers (ALs). Modelling of ellipsometry spectra shows substantial changes in inhomogeneity and optical constants of BHJ ALs with P3HT-NW inclusion. Furthermore, finite-difference time-domain simulation results based on actual device structures with inhomogeneous AL models indicate that enhanced light harvesting is a main contributing factor to efficiency improvement. On the contrary, P3HT-NW inclusion has no significant effect on charge carrier collection, other than suppressing occurrence of cul-de-sac in hole-transport pathways and unfavourable indene-C60 bisadduct domains near top anodes.

© 2017 Elsevier B.V. All rights reserved.

## 1. Introduction

Poly(3-hexylthiophene-2,5-diyl) nanowires (P3HT NWs) derived from  $\pi$ - $\pi$  stacking of P3HT polymer chains has attracted great interest since the first report on precipitation from a saturated chloroform (CF) solution of P3HT by Cho et al. [1] Focus of interest has been substitution of P3HT NWs for pristine P3HT in bulk heterojunction (BHJ) organic solar cells (OSCs). One dimensional (1D) structure is natural for network morphology. Consequently, P3HT NWs are advantageous in maximizing junctional area between electron-donating P3HT NWs and electron-accepting fullerene derivatives in active layers (ALs), without interrupting continuous hole- and electron-transport pathways [2]. In particular, high mobility P3HT NWs in the order of ~20 nm in diameter can be optimal because of limited exciton diffusion length of 10–20 nm. P3HT NWs' high charge mobility is linked to 1D crystalline

structure [1,3]. Indeed, charge mobility of single crystalline P3HT NWs was reported to be 60 times higher than that of spin-coated P3HT films [4,5].

There were previous reports on fabrication of BHJ organic solar cells (OSCs) based on P3HT 1D structures [5–10]. For example, Cho et al. reported fabrication of BHJ OSCs with P3HT NWs and electron-accepting [6,6]-phenyl-C61-butyric acid methyl ester (PCBM). They reported power conversion efficiency (PCE) as high as 3.9% with sufficiently aged (>60 h) P3HT NWs [7]. Both Guillerez et al. and Betho et al. used P3HT nanofibers prepared from *p*-xylene solution together with PCBM to fabricate BHJs OSCs that showed respective PCEs of 3.6% and 3.2% [11,12]. Xie et al. fabricated BHJ OSCs with additional P3HT nanofibrils in ALs, which were induced by adding small amount of acetone to P3HT solution in chlorobenzene [13]. Yang et al. added hexane to dichlorobenzene (DCB) solution to improve P3HT crystallinity by forming numerous fibrillar P3HT crystals, and achieved PCE of 3.9% from their P3HT:PCBM OSCs [14]. On the other hand, Kim et al. used P3HT NWs prepared by ultrasonic-assisted self-assembly with PCBM to fabricate BHJ OSCs. They achieved PCE of 4.09% after thermal annealing when highly regioregular P3HT was used [15].

\* Corresponding author. Department of Physics and Department of Energy Systems Research, Ajou University, South Korea

E-mail address: [soonil@ajou.ac.kr](mailto:soonil@ajou.ac.kr) (S. Lee).

Except one known example that reported low PCE [16], all previously reported BHJ OSCs based on 1D P3HT nanostructures were fabricated by using PCBM, the most popular acceptor material. In this work, we replaced PCBM with indene-C60 bisadduct (ICBA), another electron acceptor [17]. ICBA is advantageous for higher open-circuit voltage ( $V_{oc}$ ) because unoccupied molecular level (LUMO) of ICBA lies above that of PCBM [17–19]. Another noticeable difference is their surface energies. Compared to surface energy of pristine P3HT ( $26.42 \text{ mJ m}^{-2}$ ), those of ICBA ( $21.71 \text{ mJ m}^{-2}$ ) and PCBM ( $31.74 \text{ mJ m}^{-2}$ ) are smaller and larger, respectively [20]. Surface energy difference between donor and acceptor materials is one of the driving forces for vertical phase separation that critically affects device operation. For example, donor (acceptor) domains in the vicinity of cathode (anode) can be detrimental to BHJ OSC operation because mismatch between charge carriers and electrodes result in recombination losses. On the other hand, interdigitated morphology of high mobility P3HT NWs and continuous electron-acceptor vertical domains is ideal for ALs from a highly simplified view [21].

There is no doubt that knowledge of vertical inhomogeneity and/or phase separation is important to develop efficient BHJ OSCs. Surprisingly, previous papers on BHJ OSCs based on P3HT 1D nanostructures hardly discussed such issues. In this work, we used modelling analysis of ellipsometry spectra to manifest vertical inhomogeneity in BHJ ALs of pre-formed P3HT NWs and ICBA. Moreover, we utilized finite-difference time-domain (FDTD) simulations based on actual device structure and inhomogeneous AL models to estimate net light harvesting efficiency (LHE) free from parasitic contributions. Such LHE spectra were then used to deduce internal quantum efficiency (IQE) from measured external quantum efficiency (EQE) [22,23]. Variations in LHE and IQE spectra, together with equivalent-circuit parameters deduced from measured current density-versus-voltage ( $J$ - $V$ ) curves, were useful to separate optical and electrical contributions of P3HT-NW inclusion to device PCE improvements.

## 2. Results and discussion

Normal BHJ active layers were spin-coated from a 1:1 mixture of DCB solutions of P3HT ( $17 \text{ mg mL}^{-1}$ ) and ICBA ( $17 \text{ mg mL}^{-1}$ ). Novel BHJ layers with P3HT-NW inclusion were cast from another solution that was an equal-volume mixture of an ICBA solution in DCB ( $17 \text{ mg mL}^{-1}$ ) and a stock solution containing both pristine P3HT and P3HT NWs in a mixed solvent of DCB and dichloromethane (DCM). The stock solution was prepared in two steps (See Supporting Information, Fig. S1). Firstly, P3HT NWs were formed by taking advantage of the temperature dependence of P3HT solubility in DCM [24,25]. Cooling down a P3HT solution in DCM ( $4 \text{ mg mL}^{-1}$ ) from  $60^\circ\text{C}$  to room temperature ( $\sim 22^\circ\text{C}$ ) resulted in precipitation of P3HT NWs [7]. Secondly, an equal volume of P3HT solution in DCB ( $24 \text{ mg mL}^{-1}$ ) was added to the dispersion of precipitated P3HT NWs in DCM ( $4 \text{ mg mL}^{-1}$ ) and thoroughly mixed for 12 h to complete stock-solution preparation. The fraction of NWs in P3HT solute was 16.7% for the stock solution of pristine P3HT and P3HT NWs in mixed DCM and DCB.

Fig. 1(a) is a typical atomic force microscopy (AFM) image of P3HT NWs cast from a diluted dispersion solution of precipitated P3HT NWs in DCM. Length measurements of 100 P3HT NWs from a high resolution AFM image revealed that more than 90% of P3HT NWs were longer than  $1.0 \mu\text{m}$ . The average length of P3HT NWs estimated from the lognormal distribution in Fig. 1(b) was  $1.47 \pm 0.46 \mu\text{m}$ . It is worth emphasizing that the precipitated P3HT NWs remained intact in the stock solution such that P3HT NWs were clearly visible on AFM and transmission electron microscopy (TEM) images of films cast either from the stock solution or the

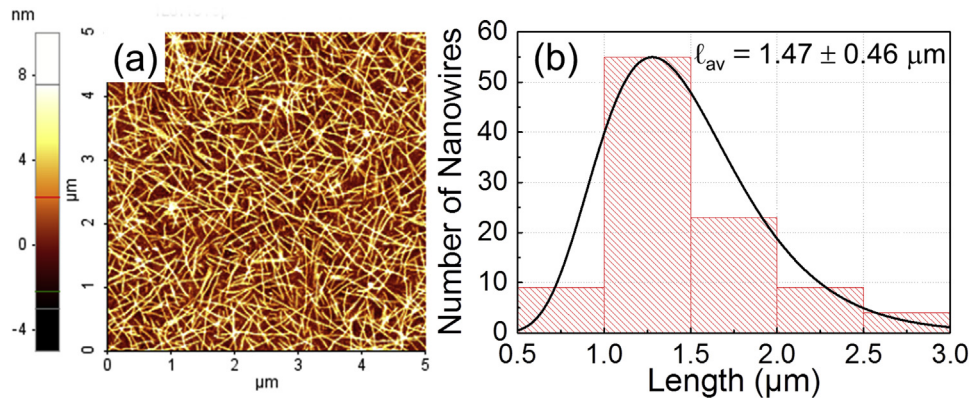
equal volume mixture of the stock solution and the ICBA solution in DCB (Supporting Information, Fig. S2).

Fig. 2 shows  $J$ - $V$  characteristics of BHJ solar cells, active layers of which consisted of P3HT donor and ICBA acceptor. Two (conventional or inverted) device structures that use ITO as either an anode or a cathode (Supporting Information, Fig. S3) were combined with either a normal or a novel (with P3HT-NW inclusion) active layer to fabricate four types of solar cells. Main performance parameters extracted from the best-fitting curves to an equivalent circuit model based on a non-ideal diode with parasitic resistances, series resistance  $R_s$  and shunt resistance  $R_{sh}$  [26–28], are summarized in Table 1 (Supporting Information, Fig. S4). We note that P3HT-NW inclusion led to all-round improvements in device operation regardless of their structures. Specifically, 4.50% (from 8.22 to  $8.59 \text{ mA cm}^{-2}$ ) improvement in short-circuit current ( $J_{sc}$ ), 3.29% (from 0.761 to 0.786 V) in  $V_{oc}$ , 4.97% (from 0.523 to 0.549) in fill factor (FF), and, consequently, 13.5% (from 3.27 to 3.71%) in PCE were observed from conventional-structure devices. Similar overall improvements appeared from inverted-structure devices in response to P3HT-NW inclusion, but with a less prominent PCE increase of 8.58%, (from 4.43% to 4.81%) because of smaller improvements in  $J_{sc}$  (from 9.41 to  $9.60 \text{ mA cm}^{-2}$ ),  $V_{oc}$  (from 0.787 to 0.811 V), and FF (from 0.596 to 0.618).

Such observations led us to conclude that the inclusion of P3HT NWs in a BHJ active layer was an efficient and universal way to enhance the performance of P3HT:ICBA solar cells. Another interesting observation was that PCE improvements resulted from structural modification were larger than those induced by P3HT-NW inclusion. Specifically, PCE increased by 35.5% and 29.6% for devices having normal (without P3HT-NW inclusion) and novel (with P3HT-NW inclusion) active layers, respectively, in response to change from a conventional to an inverted structure. Naturally, the combination of an inverted structure and P3HT-NW inclusion resulted in a dramatic PCE increase of 47.1%, from 3.27% of C-BHJ to 4.81% of I-BHJ-NW.

To elucidate how P3HT NWs contributed to the aforementioned improvements, we measured EQE variations with respect to photon wavelength, which are equivalent to incident photon-to-current conversion (IPCE) spectra. IPCE and incremental  $J_{sc}$  spectra in Fig. 3 show that the larger  $J_{sc}$  of inverted-structure devices originated from more efficient conversion of photons in the wavelength range from 465 to 645 nm. More specifically, high EQE corresponds to larger LHE and/or high IQE [22,23,29]. Basically, AL absorbance and LHE are equivalent because photons lost by reflection or absorbed by other constituent layers do not contribute to currents. We isolated AL absorbance spectra of the four devices by carrying out FDTD simulations based on their respective multilayer architectures. An indispensable prerequisite for FDTD simulation was collecting optical constants for each constituent layers. Optical constants of all other layers except ALs were available from literature. However, optical constants of two types of P3HT:ICBA BHJ ALs, with or without P3HT NW inclusion, were extracted from analysis of ellipsometric spectra.

We were unable to fit measured ellipsometric spectra assuming uniform ALs, but modelling of non-uniform ALs as 7 sublayers resulted in very good agreement between measured and simulated spectra as shown in Fig. 4 (see Supporting Information for details of modelling). Each sublayer was treated as an effective medium that consisted of a pseudo BHJ-AL material (with or without P3HT-NW inclusion) and void. Accordingly, optical constants of sublayers were calculated by using Bruggeman's effective medium theory [30,31] (Supporting Information, Fig. S5). Fig. 5 shows optical constants of pseudo BHJ-AL materials and void distributions in both ALs corresponding to the best-fitting curves in Fig. 4. Slightly larger  $n$  and lower void fractions indicate that novel ALs with P3HT-NW



**Fig. 1.** (a) AFM image of a typical film cast from a 1-mg/ml solution of P3HT NWs in DCM. The original P3HT-NW stock solution can be diluted by adding more DCM. (b) Length distribution of P3HT NWs. A high resolution AFM image was used for length measurement of 100 P3HT NWs that were cast on a silicon substrate from a highly diluted solution. The average length of P3HT NWs, corresponding to a lognormal distribution (solid black line), is  $1.47 \pm 0.46 \mu\text{m}$ .

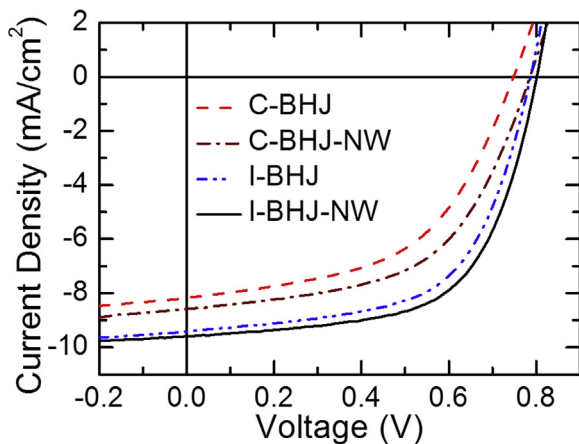


**Fig. 2.** *J-V* characteristics of the P3HT:ICBA BHJ solar cells under AM 1.5G solar illumination. C-BHJ and C-BHJ-NW are the devices with a conventional structure (ITO/PEDOT:PSS/active layer/LiF/Al) and I-BHJ and I-BHJ-NW are the ones with an inverted structure (ITO/ZnO/active layer/MoO<sub>3</sub>/Ag). The active layers of C-BHJ-NW and I-BHJ-NW contain P3HT NWs.

inclusion were denser compared to normal ALs. Moreover, larger  $k$  in visible wavelength range made novel ALs more effective in harvesting visible wavelength photons. Difference in void-fraction variations is another noticeable feature. P3HT-NW inclusion apparently made ALs not only denser but also less inhomogeneous. It seems that long P3HT NWs were randomly intertwined and ICBA and/or pristine P3HT occupied spaces among P3HT NWs. Consequently, BHJs were spread throughout the depth of ALs so that less inhomogeneous and more efficient ALs were formed. On the contrary, void-fraction gradation of normal ALs having no P3HT NWs appears consistent with a common view that midsection BHJs were sandwiched between P3HT- and ICBA-rich regions.

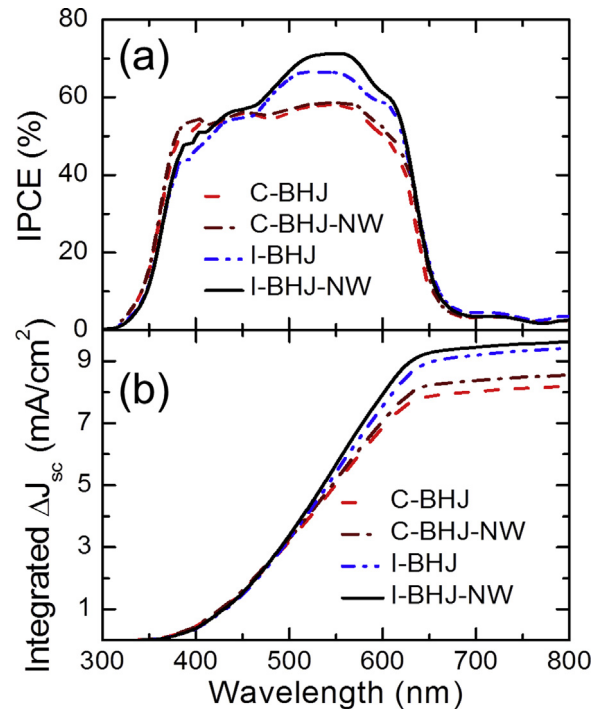


**Fig. 3.** (a) Comparison of IPCE spectra of the four types of P3HT:ICBA BHJ solar cells. IPCE spectra of structurally identical (either conventional or inverted) devices are similar regardless of active layer types (with or without P3HT NW inclusion). However, there is a noticeable difference in IPCE spectra between two device structures regardless of active layer types. (b) Integrated  $\Delta J_{sc}(\lambda)$  represent accumulated currents due to solar irradiance below wavelength  $\lambda$ . The contributions of solar photons up to 800 nm produce  $J_{sc}$  values that closely match measured ones.

**Fig. 6** shows light absorbance spectra of ALs in four P3HT:ICBA BHJ solar cells. These spectra were extracted from FDTD simulations

**Table 1**

Device characteristics of P3HT:ICBA bulk-heterojunction (BHJ) solar cells with and without P3HT-NW inclusion in active layers. Two devices have a conventional structure with a bottom ITO anode (ITO/PEDOT:PSS/active layer/LiF/Al) and the other two have an inverted structure with a top Ag anode (ITO/ZnO/active layer/MoO<sub>3</sub>/Ag). The effective cell area is  $0.24 \text{ cm}^2$  for these devices. The active layers of C-BHJ-NW and I-BHJ-NW contain P3HT NWs.

Sample ID	P3HT NW inclusion	$V_{oc}$ (V)	$J_{sc}$ (mA/cm <sup>2</sup> )	FF (%)	$R_s$ ( $\Omega \text{ cm}^2$ )	$R_{sh}$ ( $\Omega \text{ cm}^2$ )	PCE (%)
C-BHJ	no	0.761	8.22	52.3	$13.2 \pm 0.03$	$451 \pm 3.43$	3.27
C-BHJ-NW	yes	0.786	8.59	54.9	$10.9 \pm 0.02$	$486 \pm 6.84$	3.71
I-BHJ	no	0.787	9.41	59.8	$1.67 \pm 0.03$	$717 \pm 12.0$	4.43
I-BHJ-NW	yes	0.811	9.60	61.8	$1.87 \pm 0.03$	$916 \pm 12.0$	4.81

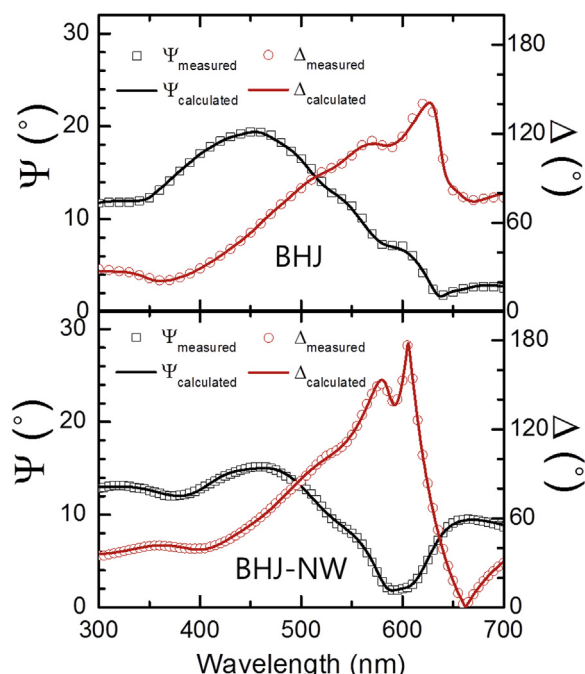


**Fig. 4.** Ellipsometric spectra of two types of active layers, with or without P3HT NW inclusion. Solid squares and circles represent measured  $\Psi$  and  $\Delta$  spectra, respectively. Solid lines are corresponding best-fitting curves based on inhomogeneous sublayer modelling.

with actual device structures, which automatically took into account full multilayer optical effects and allowed separation of absorbance spectrum for any constituent layer. Concomitant determination of absorbance spectra of other layers showed appreciable contributions of such parasitic components to total absorbance spectra (Supporting Information, Fig. S6). LHE estimation from device reflectance and/or ALs' extinction coefficients tends to be inaccurate because parasitic absorbance contributions

and multilayer optical effects are neglected. On the contrary, we were able to utilize parasitic absorbance spectra to verify validity of our FDTD simulation results and inhomogeneous AL models. From energy conservation, the sum of reflectance and absorbance should be 1 for opaque devices. Therefore, reflectance spectra of opaque devices can be calculated from the sum of AL and parasitic absorbance spectra:

$$R_{Device}(\lambda) = 1 - A_{AL}(\lambda) - A_{parasitic}(\lambda). \quad (1)$$

Good agreement between measured and calculated reflectance spectra of four opaque solar cells in Fig. 7 confirms that our FDTD simulations with inhomogeneous AL models were successful in deducing LHE spectra of four P3HT:ICBA BHJ solar cells.

IQE spectra that we calculated by combining LHE and IPCE spectra are shown in Fig. 8:

$$IQE(\lambda) = IPCE(\lambda)/LHE(\lambda). \quad (2)$$

Surprisingly, P3HT-NW inclusion resulted in IQE decrease for conventional-structure devices, and similar IQE decrease was induced when device structure was inverted without P3HT-NW inclusion. However, inclusion of P3HT NWs resulted in IQE increase for inverted structure devices. More significant changes appeared among LHE spectra. LHEs of C-BHJ device, which were particularly low, were noticeably improved as a result of P3HT-NW inclusion. Similar LHE improvement occurred without P3HT inclusion when device structure was inverted. Moreover, combination of device structure inversion and P3HT-NW inclusion resulted in even higher LHEs. We argue that inclusion of P3HT NWs was not necessarily advantageous for charge carrier collection because P3HT NWs were about 7 times longer than typical AL thickness. On the contrary, aforementioned larger  $k$  and reduced inhomogeneity of ALs induced by P3HT-NW inclusion were more significant factors for PCE improvements.

Finally, we propose that variations in AL morphology and device structure resulted in the systematic difference in two parasitic resistances listed in Table 1. First, 6–8 times smaller  $R_S$  of inverted structure devices must be linked to optimal use of charge

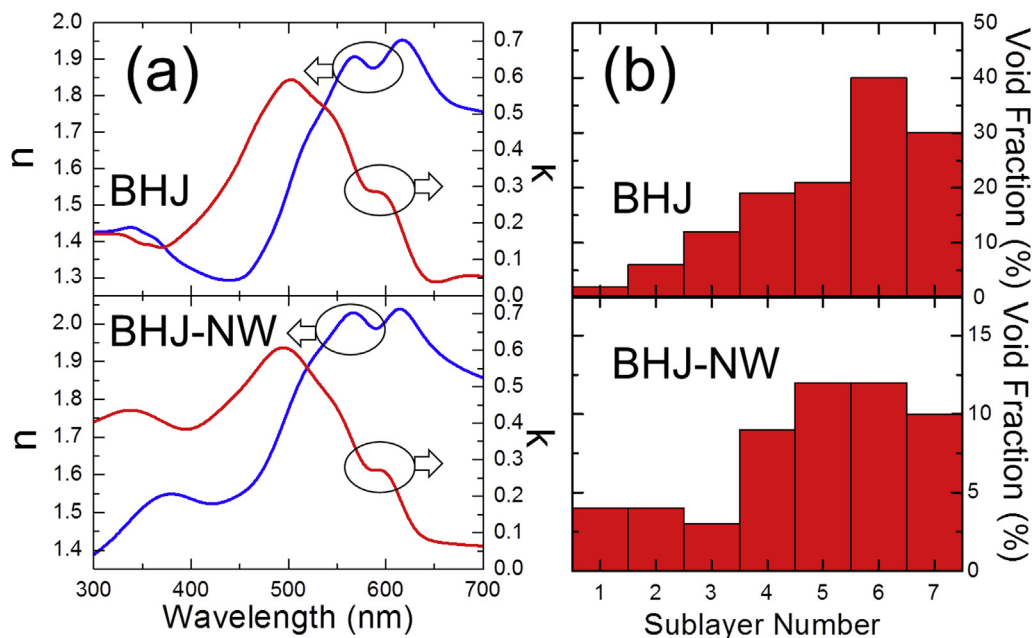


**Fig. 5.** Effective optical constants (a) and void distributions (b) of two types of active layers (with and without P3HT NW inclusion) corresponding to the best-fitting curves in Fig. 4. Both types of active layers were represented by seven sublayers to represent nonuniformity along depth.

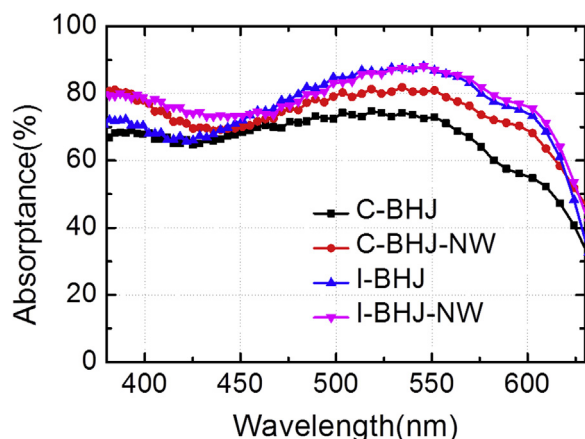


Fig. 6. Comparison of light absorbance of active layers in four types of P3HT:ICBA BHJ solar cells. Only photons absorbed by active layers are converted into currents.

transporting metal-oxide junction layers. By using ZnO and MoO<sub>3</sub> as cathodic and anodic junction layers, respectively, charge-carrier extraction became more efficient. Second, 1.6–1.8 times larger  $R_{SH}$  of inverted structure devices indicates reduced recombination loss of charge carriers. Cul-de-sac in charge-carrier transport pathways and/or P3HT (ICBA) domains near cathode (anode) can be origins of charge-carrier recombination events to which photo-shunt is typically attributed. Apparently, P3HT-NW inclusion is expected to minimize cul-de-sac in hole-transport pathways. Moreover, occurrence of unfavourable ICBA domains near top anodes will be substantially reduced in the case of dense and homogeneous ALs with P3HT-NW inclusion.

### 3. Experimental section

We fabricated BHJ OSCs in two architectural configurations by using a commercially available ITO-covered glass ( $12 \Omega \text{ sq}^{-1}$ , GEOMATEC) as a substrate. In a conventional configuration of ITO/PEDOT:PSS/P3HT:ICBA/LiF/Al, ITO was an anode. On the contrary, ITO was a cathode in an inverted configuration of ITO/ZnO/P3HT:ICBA/MoO<sub>3</sub>/Ag. Two types of P3HT:ICBA ALs were formed for each OSC structure by spin-coating different mixture solutions of ICBA (SOL5064A, Solaris Chem.) and P3HT (4002-E, Rieke Metals). Normal BHJ ALs without P3HT-NW inclusion were spin-coated from a 1:1 weight-mixture solution of P3HT and ICBA in DCB at the concentration of  $34 \text{ mg mL}^{-1}$ . On the other hand, novel BHJ ALs with P3HT-NW inclusion were spin-coated from a mixture of a DCB solution of ICBA ( $17 \text{ mg mL}^{-1}$ ) and a mixed-solvent (DCM and DCB) stock solution of P3HT and P3HT NWs. The thickness of P3HT:ICBA active layers was 210 nm. Aqueous PEDOT:PSS solution (Clevios P, Heraeus) was spin-coated and annealed at  $140 \text{ }^\circ\text{C}$  for 10 min to make 30-nm thick hole-extraction layers (HELs). ZnO electron-extraction layers, thickness of which was 20 nm, were formed by spin-coating a precursor solution and then baking it at  $200 \text{ }^\circ\text{C}$  for 30 min. LiF/Al cathodes, Ag anodes, and MoO<sub>3</sub> HELs were evaporated in high vacuum ( $\sim 10^{-4} \text{ Pa}$ ). The thickness of MoO<sub>3</sub> layers was 20 nm.

The cell size, defined by the overlap of cathode and anode electrodes, was  $0.24 \text{ cm}^2$ . All devices were measured under AM 1.5G illumination at 1 sun by using a solar simulator (PEC-L01, Peccell) that was calibrated to  $100 \text{ mWcm}^{-2}$  with a reference Si cell (PEC-S101, Peccell). EQE of the fabricated OSCs was measured by using a Photo Electrochemistry IPCE system (PE-IPCE, HS Technologies). Reflectance was measured by using a spectrophotometer (Cary 5000, Varian), and  $\Delta$  and  $\Psi$  spectra were measured by using an ellipsometer (V-Vase, J. A. Woollam). Morphology of P3HT NWs and related films were examined by using an atomic force

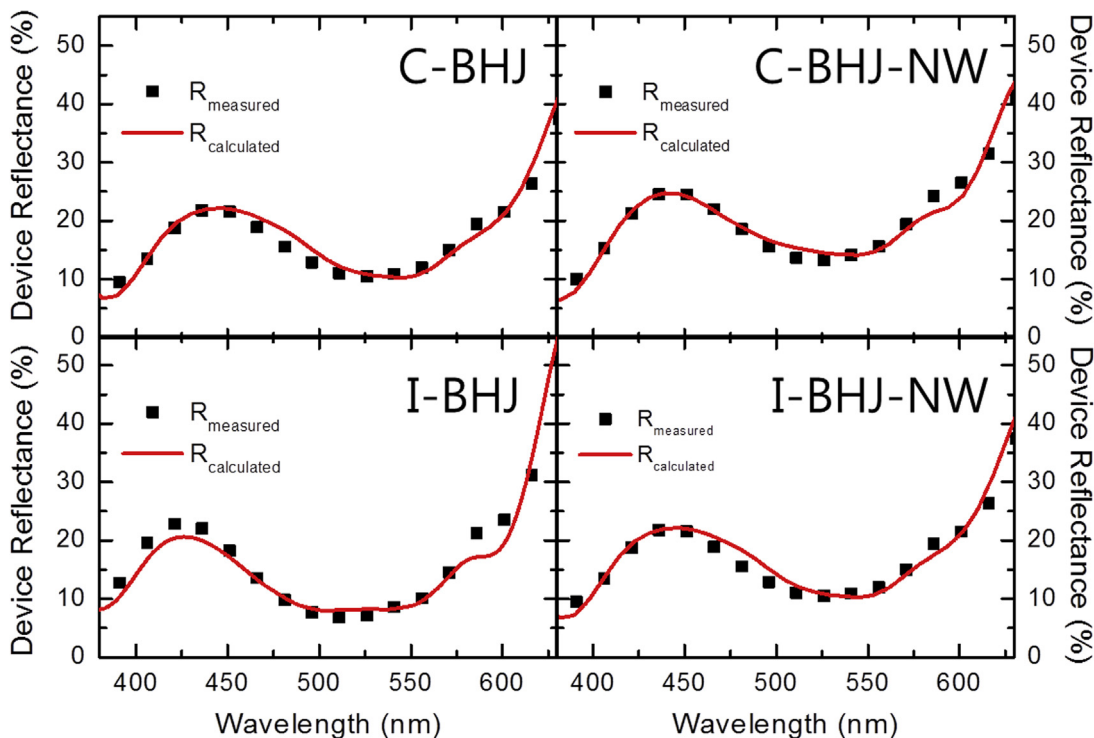
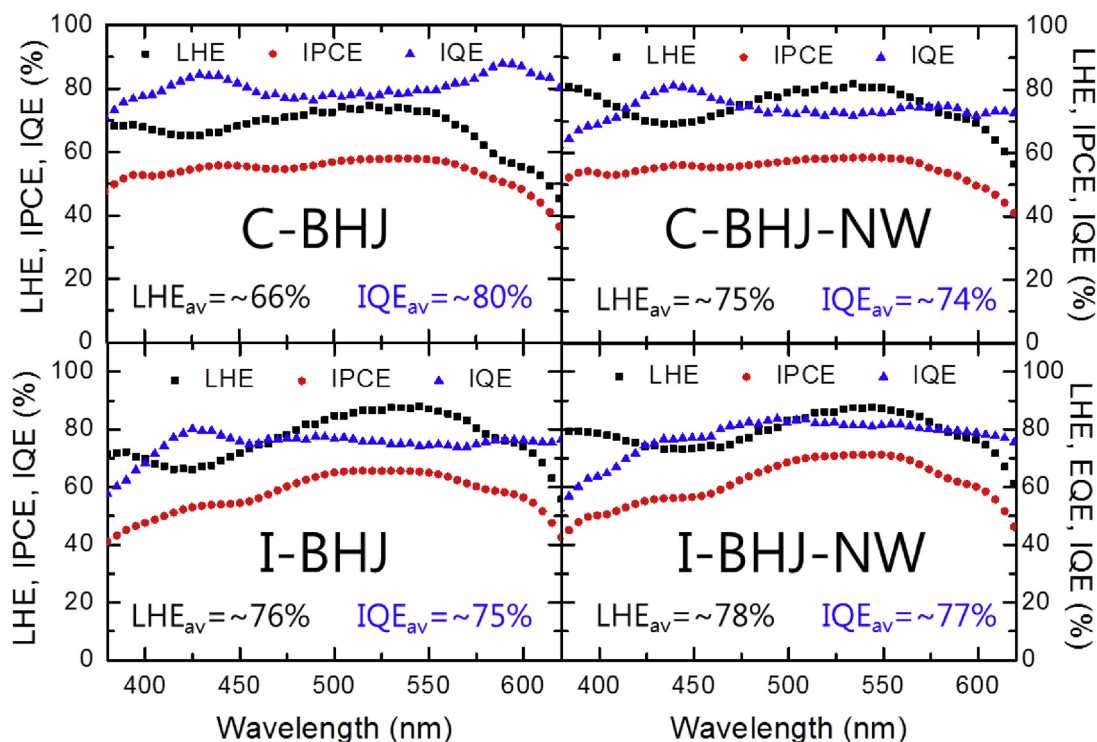


Fig. 7. Measured (solid squares) and calculated (solid lines) reflectance spectra of the four types of P3HT:ICBA BHJ solar cells. The inhomogeneous active layer models in Fig. 5 were used in calculating reflectance spectra.



**Fig. 8.** LHE, IPCE, and IQE spectra of the four types of P3HT:ICBA BHJ solar cells.  $IQE(\lambda)$  was deduced from  $EQE(\lambda)$  and  $LHE(\lambda)$ :  $IQE(\lambda) = EQE(\lambda)/LHE(\lambda)$ . It is interesting to note that the inclusion of P3HT NWs contributed to LHE improvements regardless of device structures. However, LHE increase was much more prominent in the case of a conventional structure. On the contrary, P3HT-NW inclusion resulted in opposite IQE changes: a slight increase for the inverted structure, but a significant decrease for the conventional structure.

microscope (XE-100, Park system) and a transmission electron microscope (JEM-2100F, JEOL). A commercial program (FDTD Solutions, Lumerical Software) was used to perform FDTD simulations. To separate AL absorbance from parasitic contributions of other layers, we placed ‘Intensity Monitor’ at each interface between adjacent layers.

#### 4. Conclusion

In conclusion, P3HT NWs, pre-made by dropping the temperature of a P3HT solution in DCM below a precipitation point, were used to modify formation and distribution of BHJs between P3HT and ICBA. Indeed, P3HT-NW inclusion in ALs was a universal and efficient recipe for PCE improvement of BHJ OSCs regardless of device architectures. Combining additional contribution from an inverted configuration with that from P3HT-NW inclusion, we were able to improve PCE by 47.1% from that of a common device. Modelling analysis of ellipsometric spectra and FDTD simulations based on realistic device structures showed that substantial changes in inhomogeneity, and effective optical constants of BHJ ALs occurred in response of P3HT-NW inclusion. Consequently, large difference in light harvesting efficiency followed. IQE estimated by taking into account only AL absorbance, which were separated from all other parasitic contributions in FDTD simulation results, showed that P3HT-NW inclusion has no significant effects on charge carrier collection, other than reducing cul-de-sac in hole-transport pathways and unfavourable ICBA domains near top anodes. In short, nanostructures of ALs including randomly intertwined long (>1  $\mu\text{m}$ ) P3HT NWs are far from ideal fin-like morphology [2,21,32,33]. Nevertheless, utilization of preformed P3HT wires is a viable option for optimization of BHJ solar cells because elaborate manipulation of vertical inhomogeneity of ALs is feasible with sequential coating of different P3HT-NW

concentration stock solutions. Unlike pristine P3HT, preformed P3HT NWs remain intact during subsequent exposure to solvents.

#### Acknowledgment

This research was supported by the National Research Foundation of Korea Grant (No. NRF-535 2014R1A2A2A01005632) which is funded by the Korea government (MEST), and through the Priority Research Centers Program (NRF2009e0094046).

#### Appendix A. Supplementary data

Supplementary data related to this article can be found at <http://dx.doi.org/10.1016/j.orgel.2016.12.063>.

#### References

- [1] B. Do, H. Kim, J.T. Han, Y.D. Park, Y. Jang, J.H. Cho, M. Hwang, K. Cho, Single-crystal polythiophene microwires grown by self-assembly, *Adv. Mater.* 18 (6) (2006) 719–723.
- [2] J.H. Kim, M. Kim, H. Jinnai, T.J. Shin, H. Kim, J.H. Park, S.B. Jo, K. Cho, Organic solar cells based on three-dimensionally percolated polythiophene nanowires with enhanced charge transport, *ACS Appl. Mater. Interfaces* 6 (8) (2014) 5640–5650.
- [3] J.A. Merlo, C.D. Frisbie, Field effect transport and trapping in regioregular polythiophene nanofibers, *J. Phys. Chem. B* 108 (50) (2004) 19169–19179.
- [4] J.A. Merlo, C.D. Frisbie, Field effect conductance of conducting polymer nanofibers, *J. Polym. Sci. Part B - Polym. Phys.* 41 (21) (2003) 2674.
- [5] J.-H. Kim, J.H. Park, J.H. Lee, J.S. Kim, M. Sim, C. Shim, K. Cho, Bulk heterojunction solar cells based on preformed polythiophene nanowires via solubility-induced crystallization, *J. Mater. Chem.* 20 (2010) 7398.
- [6] Y. Yao, J. Hou, Z. Xu, G. Li, Y. Yang, Effects of solvent mixtures on the nanoscale phase separation in polymer solar cells, *Adv. Funct. Mater.* 18 (12) (2008) 1783–1789.
- [7] J.S. Kim, J.H. Lee, J.H. Park, C. Shim, M. Sim, K. Cho, High-efficiency organic solar cells based on preformed poly(3-hexylthiophene) nanowires, *Adv. Funct. Mater.* 21 (3) (2011) 480–486.
- [8] J.F. Chang, B. Sun, D.W. Breiby, M.M. Nielsen, T.I. Sølling, M. Giles, I. McCulloch,

- H. Sirringhaus, Enhanced mobility of poly(3-hexylthiophene) transistors by spin-coating from high-boiling-point solvents, *Chem. Mater.* 16 (23) (2004) 4772–4776.
- [9] D. Moerman, R. Lazzaroni, O. Douhéret, Efficient bulk heterojunction photovoltaic cells with a pre-organized poly(3-hexylthiophene) phase, *Appl. Phys. Lett.* 99 (9) (2011) 1–4.
- [10] J.Y. Oh, M. Shin, T.I. Lee, W.S. Jang, Y. Min, J.M. Myoung, H.K. Baik, U. Jeong, Self-seeded growth of poly(3-hexylthiophene) (P3HT) nanofibrils by a cycle of cooling and heating in solutions, *Macromolecules* 45 (18) (2012) 7504–7513.
- [11] S. Berson, R. De Bettignies, S. Bailly, S. Guillerez, Poly(3-Hexylthiophene) fibers for photovoltaic applications, *Adv. Funct. Mater.* 17 (8) (2007) 1377–1384.
- [12] S. Bertho, W.D. Oosterbaan, V. Vrindts, J. D'Haen, T.J. Cleij, L. Lutsen, J. Manca, D. Vanderzande, Controlling the morphology of nanofiber-P3HT: PCBM blends for organic bulk heterojunction solar cells, *Org. Electron. Phys. Mater. Appl.* 10 (7) (2009) 1248–1251.
- [13] Y. Zhao, S. Shao, Z. Xie, Y. Geng, L. Wang, Effect of poly (3-Hexylthiophene) nanofibrils on charge separation and transport in polymer bulk heterojunction photovoltaic cells, *J. Phys. Chem. C* 113 (39) (2009) 17235–17239.
- [14] L. Li, G. Lu, X. Yang, Improving performance of polymer photovoltaic devices using an annealing-free approach via construction of ordered aggregates in solution, *J. Mater. Chem.* 18 (17) (2008) 1984–1990.
- [15] B.G. Kim, M.S. Kim, J. Kim, Ultrasonic-assisted nanodimensional self-assembly of poly-3-hexylthiophene for organic photovoltaic cells, *ACS Nano* 4 (4) (2010) 2160–2166.
- [16] T. Salim, S. Sun, L.H. Wong, L. Xi, Y.L. Foo, Y.M. Lam, The role of poly(3-hexylthiophene) nanofibers in an all-polymer blend with a polyfluorene copolymer for solar cell applications, *J. Phys. Chem. C* 114 (20) (2010) 9459–9468.
- [17] Y. He, H.Y. Chen, J. Hou, Y. Li, Indene – C60 bisadduct: a new acceptor for high-performance polymer solar cells, *J. Am. Chem. Soc.* 132 (4) (2010) 1377–1382.
- [18] Darin W. Laird, Reza Stegamat, Henning Richter, Viktor Vejins, Larry Scott, T. A. L. Organic Photovoltaic Devices Comprising Fullerenes and Derivatives Thereof. WO2008018931 A2, 2008.
- [19] C.Y. Chang, C.E. Wu, S.Y. Chen, C. Cui, Y.J. Cheng, C.S. Hsu, Y.L. Wang, Y. Li, Enhanced performance and stability of a polymer solar cell by incorporation of vertically aligned, cross-linked fullerene nanorods, *Angew. Chem. - Int. Ed.* 50 (40) (2011) 9386–9390.
- [20] J.H. Huang, Y.S. Hsiao, E. Richard, C.C. Chen, P. Chen, G. Li, C.W. Chu, Y. Yang, The investigation of donor-acceptor compatibility in bulk-heterojunction polymer systems, *Appl. Phys. Lett.* 103 (4) (2013) 1–5.
- [21] S. Günes, H. Neugebauer, N.S. Sariciftci, Conjugated polymer-based organic solar cells, *Chem. Rev.* 107 (4) (2007) 1324–1338.
- [22] Z. He, C. Zhong, S. Su, M. Xu, H. Wu, Y. Cao, Enhanced power-conversion efficiency in polymer solar cells using an inverted device structure, *Nat. Photonics* 6 (9) (2012) 593–597.
- [23] J. Burschka, N. Pellet, S.-J. Moon, R. Humphry-Baker, P. Gao, M.K. Nazeeruddin, M. Grätzel, Sequential deposition as a route to high-performance perovskite-sensitized solar cells, *Nature* 499 (7458) (2013) 316–320.
- [24] L. Qiu, W.H. Lee, X. Wang, J.S. Kim, J.A. Lim, D. Kwak, S. Lee, K. Cho, Organic thin-film transistors based on polythiophene nanowires embedded in insulating polymer, *Adv. Mater.* 21 (13) (2009) 1349–1353.
- [25] L. Qiu, X. Wang, W.H. Lee, J.A. Lim, J.S. Kim, D. Kwak, K. Cho, Organic thin-film transistors based on blends of poly(3-hexylthiophene) and polystyrene with a solubility-induced low percolation threshold, *Chem. Mater.* 21 (19) (2009) 4380–4386.
- [26] B. Kippelen, J.-L. Brédas, J.-L. Br Edas, Organic photovoltaics, *Energy Environ. Sci.* 2 (3) (2009) 251.
- [27] J.D. Servaites, S. Yeganeh, T.J. Marks, M.A. Ratner, Efficiency enhancement in organic photovoltaic cells: consequences of optimizing series resistance, *Adv. Funct. Mater.* 20 (1) (2010) 97–104.
- [28] J.H. Yim, S.Y. Joe, C. Pang, K.M. Lee, H. Jeong, J.Y. Park, Y.H. Ahn, J.C. De Mello, S. Lee, Fully solution-processed semitransparent organic solar cells with a silver nanowire cathode and a conducting polymer anode, *ACS Nano* 8 (3) (2014) 2857–2863.
- [29] S.Y. Joe, J.H. Yim, S.Y. Ryu, N.Y. Ha, Y.H. Ahn, J.Y. Park, S. Lee, Universal efficiency improvement in organic solar cells based on a poly(3-hexylthiophene) donor and an indene-C<sub>60</sub> bisadduct acceptor with additional donor nanowires, *ChemPhysChem* 16 (6) (2015) 1217–1222.
- [30] D.A.G. Bruggeman, Berechnung Verschiedener Physikalischer Konstanten von Heterogenen Substanzen. I. Dielektrizitätskonstanten Und Leitfähigkeiten Der Mischkörper Aus Isotropen Substanzen, *Ann. Phys.* 416 (7) (1935) 636–664.
- [31] S. Lee, S.Y. Han, S.G. Oh, Spectro-ellipsometric studies of defective diamond films deposited by MPECVD, *Surf. Coat. Technol.* 112 (1–3) (1999) 194–198.
- [32] V.S. Gevaerts, L.J.A. Koster, M.M. Wienk, R.A.J. Janssen, Discriminating between bilayer and bulk heterojunction polymer:fullerene solar cells using the external quantum efficiency, *ACS Appl. Mater. Interfaces* 3 (9) (2011) 3252–3255.
- [33] D. Chen, F. Liu, C. Wang, A. Nakahara, T.P. Russell, Bulk heterojunction photovoltaic active layers via bilayer interdiffusion, *Nano Lett.* 11 (5) (2011) 2071–2078.